THE AMERICAN SOCIETY OF MECHANICAL ENGINEERS
Three Park Avenue, New York, N.Y. 10016-5990

99-GT-387

CONTACT STRESSES IN DOVETAIL ATTACHMENTS: FINITE ELEMENT MODELING

G.B. Sinclair
Department of Mechanical Engineering
Carnegie Mellon University
Pittsburgh, PA

N.G. Comier
Department of Mechanical Engineering
Carnegie Mellon University
Pittsburgh, PA

J.H. Griffin
Department of Mechanical Engineering
Carnegie Mellon University
Pittsburgh, PA

G. Meda
Science and Technology Division
Corning Incorporated
Corning, NY

ABSTRACT

The stress analysis of dovetail attachments presents some challenges. These challenges stem from the high stress gradients near the edges of contact and from the nonlinearities attending conforming contact with friction. To meet these challenges with a finite element analysis, refined grids are needed with mesh sizes near the edges of contact of the order of one percent of the local radii of curvature there. A submodeling procedure is described which can provide grids of sufficient resolution in return for moderate computational effort. This procedure furnishes peak stresses near contact edges which are converging on a sequence of three submodel grids, and which typically do converge to within about five percent.

1. INTRODUCTION

1.1 Background and Motivation

Single tooth attachments or "dovetails" are used to secure fan and compressor blades to disks in gas turbines. A section through a typical dovetail is shown in Fig. 1(a). Herein the base of the blade is pulled as a result of the centripetal acceleration of its remainder, while it is restrained by contact with the disk on two flats (e.g., $C - C'$ in Fig. 1(a)). At the edges of these contact regions, fretting can occur when loads vary. This fretting can lead to fatigue crack initiation and ultimately to failures (e.g., in the disk at C, the blade at C'). In order to understand the failure mechanisms involved, an appreciation of the stresses occurring in these critical regions is required. The primary intent of this work is to assist in achieving such an appreciation.

The stress analysis of dovetail attachments like that in Fig. 1(a) is not without challenges. To start with, these challenges stem from resolving the *stress gradients* present. Some idea of the nature of these gradients can be obtained from classical elasticity solutions for

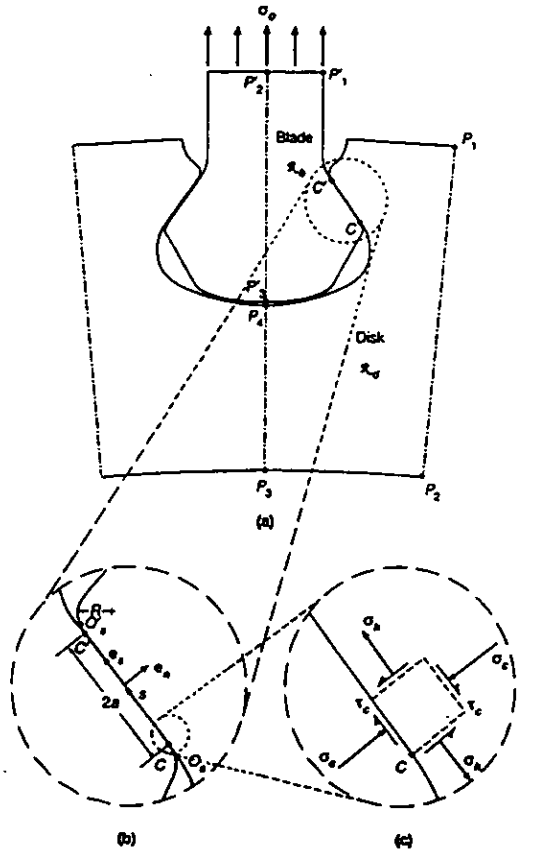

Fig. 1: Dovetail attachment configuration: (a) overall attachment, (b) close-up of contact region with local coordinates, (c) close-up of disk near lower contact point with stresses acting

Presented at the International Gas Turbine & Aeroengine Congress & Exhibition
Indianapolis, Indiana — June 7–June 10, 1999
This paper has been accepted for publication in the Transactions of the ASME
Discussion of it will be accepted at ASME Headquarters until September 30, 1999

contact by various frictionless rigid indentors. Sketched in Fig. 2(a) are sections through a cylindrical roller, a polynomial profile indentor,[1] and a flat punch with sharp corners. These indentors share a common contact extent of $2a$. Companion stresses for frictionless contact are given in Hertz (1882), Steuermann (1939) and Sadowsky (1928), respectively. These are plotted in Fig. 2(b) wherein σ_c is the contact stress and is positive when compressive (Fig. 1(b), (c)), while $\bar{\sigma}_c$ is its mean value throughout the contact region. Evident in Fig. 2(b) are the increases in stress gradients that attend smaller radii of curvature at the edges of contact. If R is the local radius of curvature (as in Fig. 1(b)), then $R/a > 1$ for the roller, $R/a \approx 1$ for the polynomial profile, and $R/a = 0$ for the flat sharp indentor. For dovetail attachments like that of Fig. 1(a), typically $1/4 < R/a < 1$ (the left-hand side of a dnvetail with $R/a = 1/2$ is shown as a broken line in Fig. 2(a)). Hence stress gradients for dovetail attachments can be expected to be between that of the polynomial profile indentor and that of the flat punch with sharp edges. The first of these has a stress concentration factor of 1.5 in Fig. 2(b), the second, with its stress singularity, an infinite stress concentration factor. Thus dovetail attachments can not oaly have high stress concentration factors, but there is also a wide range of values such factors can take on.

There are further sources of challenge in the stress analysis of dovetail attachments. These stem from the *nonlinearities* present. The first of these is the geometric nonlinearity associated with expanding contact regions when contact is conforming (as at C, C' in Fig. 1(a)). Tracking the extent of contact is essential if accurate finite stresses are to result. The second of these stems from the conditional nature of boundary conditions under an Amonton's law for friction (also referred to as Coulomb's law). Complying with this law is vital since associated contact shears τ_c largely govern values of the hoop stress σ_h (Fig. 1(c)), and it is the hoop stress that can be expected to be a major contributor to fatigue failure at the edge of contact.

1.2 Literature Search

The stress analysis of dovetail attachments belongs to a class of problems in solid mechanics commonly termed *contact problems*. A good description of the analysis of such problems, especially via complex variable techniques, is given in Gladwell (1980). A first-rate description of their analysis and physics is given in Johnson (1985) (see, in particular, Ch. 13 which describes when Amonton's law is physically applicable). A well-organized review of research in the area through 1975 is given in Kalker (1977). Further contributions to the literature through 1984 can be obtained from the extensive list of references in Johnson (1985). Papers since 1984 treating conforming contact/numerical analysis of contact problems may be found in Meda and Sinclair (1996).

Turning to the literature which specifically addresses the stress analysis of dovetail attachments, we focus on those using finite element analysis (FEA). This is because the complexity of such configurations dictates the use of numerical methods, and because, of the numerical methods available, the finite element method is arguably the most adaptable and the most widely used in industry.

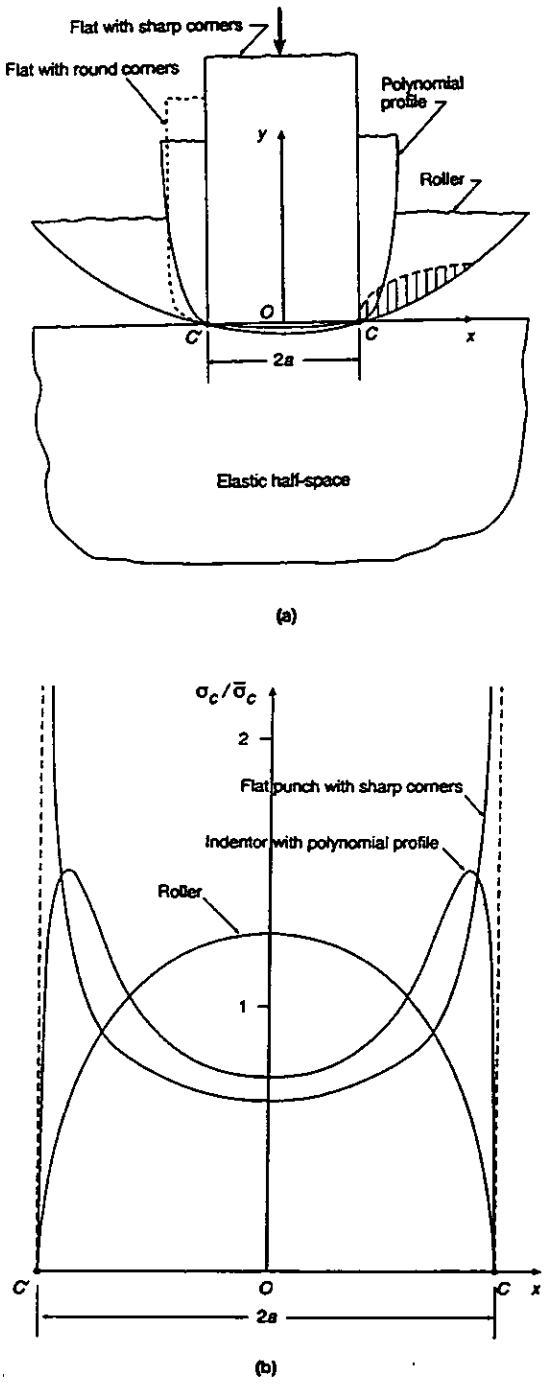

Fig. 2: Examples of contact problems:
(a) indentor profiles, (b) contact stresses

There are several papers which describe finite element analysis of dovetail attachments. An early contribution is Boddington et al.

[1] In terms of the rectangular coordinates of Fig. 2(a), the particular polynomial profile shown therein has $y/a = [(x/a)^8 - 1]/16$.

(1985) which considers two-dimensional elastic analysis. This paper explores the feasibility of implementing Amonton's law with finite elements and is successful in devising an approach for doing this. Such a capability is now available in standard codes (e.g., ANSYS, 1995). Other papers which include two-dimensional elastic FEA are Kenny et al. (1991), Papanikos and Meguid (1994), and Meguid et al. (1996). The ambitious task of a three-dimensional elastic analysis is included in Papanikos et al. (1998). While these analyses seem to be capable of computing general trends, it is questionable whether or not they have sufficient mesh refinement near the edge of contact to capture crucial local stresses in this vicinity. More precisely in this regard, if h is the length between nodes of elements used in this vicinity, theo these studies have $1/6 < h/R < 1/2$, where R continues as the local radius of curvature. It remains to be seen if such h are small enough to obtain key local stresses.

1.3 Objective and Scope

Here, then, we seek to develop an approach for obtaining the *local*, two-dimensional, elastic stresses occurring near the *edges of contact* in dovetail attachments. While a two-dimensional elastic treatment represents a simplification of the actual configuration, it is a first step in analyzing more complex models entailing three-dimensional effects and elasto-plastic flow. Further, even though simplified, two-dimensional elastic stresses can furnish a basis for understanding physics if the stresses are sufficiently accurately determined.

Critical in obtaining reasonable stress estimates is the policing of the constraints accompanying conforming contact. Only then are stresses guaranteed to be nonsingular. Thus next, in Section 2, we begin with a recap of the asymptotic arguments that establish that, properly analyzed, the conforming contact stresses of interest here are nonsingular. We summarize these arguments not only for completeness, but also because we have been given to understand that there is a diversity of opinion in the gas turbine community as to whether or not stresses in dovetail attachments are nonsingular. In addition, we wish to include a somewhat subtle but not insignificant point that is missing from these arguments in the literature.

The remainder of the paper is organized as follows. In Section 3, we describe a finite element analysis of a dovetail attachment. This FEA features a submodeling procedure which enables mesh sizes to be employed which are up to two orders of magnitude smaller than those reported in the literature. Then, in Section 4, we check that the contact stresses actually obtained comply with being nonsingular by systematically examining their convergence in some detail. We also check the policing of the friction law. We close by offering some concluding remarks in Section 5 in the light of results found.

2. CONFORMING CONTACT STRESSES

2.1 Conforming Contact Without Friction

Here by "conforming" is meant contact which, from no load to full load, has the indentor and indented material share a common tangent as the contact region's boundary is approached from outside. An example is the roller of Fig. 2(a). Initially, before any loading, the contact region for this configuration consists of a line through a single contact point. Subsequently, under loading, this point splits into C and C' as the contact region spreads (Fig. 2(a)). Throughout, contact is conforming at C (or C') in the above sense. A further example is the polynomial profile indentor of Fig. 2(a). In contrast is a sharp-edged flat punch of Fig. 2(a): this is an example of nonconforming contact at both C and C'.

In addition to assuming conforming contact to be frictionless in this subsection, we further simplify the exposition by initially considering just the rigid roller of Fig. 2(a). The local boundary conditions at C therefore take the form

$$\begin{aligned} &\sigma_y = \tau_{xy} = 0 \quad \text{on} \quad y = 0, \quad x > a, \\ &v = -v_0, \tau_{xy} = 0, \quad \text{on} \quad y = 0, \quad x < a, \end{aligned} \tag{1}$$

where σ_y, τ_{xy} are stress componeots in rectangular Cartesian coordinates (x,y) and v is the displacement in the y-direction. The first of (1) are the stress-free conditions external to the contact region. The second reflects local indentation by an amount $v_0 = v_0(x)$ without any friction within the contact region. The local fields for (1) admit to being supplemented by their fully homogeneous counterparts, namely those for (1) with $v_0 = 0$. Then we recover the classical boundary conditions for a crack, so that inverse-square-root stress singularities are possible (Williams, 1952). To remove this possibility, we add physically sensible constraints. These insist that *within the contact region* there can be *no tensile contact stresses*, whilst *without* there can be *no interpenetration or contact* between the indentor and the indented material. Thus we require

$$\begin{aligned} &\sigma_y \le 0 \quad \text{on} \quad y = 0, \quad x < a, \\ &v < \sqrt{\left[R^2 - a^2\right]} - \sqrt{\left[R^2 - x^2\right]} \quad \text{on} \quad y = 0, \quad x > a. \end{aligned} \tag{2}$$

Given compliance with these added restrictions, singular response is no longer possible.

To see this, consider what happens otherwise. There are two cases.

(i) Singular stresses participate with a positive stress intensity factor.

(ii) Singular stresses participate with a negative stress intensity factor.

Under (i), the singular stress field must dominate all others as C is approached from within the contact region, so that the contact stresses must become tensile. This is in violation of the first of (2). Under (ii), the displaced shape of the indented material just outside C is vertically upwards and consequently interpenetrates the indentor (indicated by the hatched area on the right-hand side of Fig. 2(a)). This is in violation of the second of (2). Hence the classical singular fields associated with a crack cannot participate in the conforming contact

configuration of the rigid frictionless roller if the inequality constraints of (2) are enforced.

The point that is omitted consideration in the literature is whether we can, in actuality, enforce the inequality constraints of (2) and so remove singularities. The fact that (2) would seem to be physically sensible and therefore desirable does not necessarily mean they can be enforced within classical elasticity. After all, singularities in general are nonphysical so it would be physically sensible and desirable if we could simply legislate them out of elastic solutions. Unfortunately, such legislation typically leads to the posing of a problem that has no solution, the local regular elastic fields being incomplete without their singular counterparts. For conforming contact, however, we have an additional degree of freedom of which we can take advantage. This is the extent of the contact region (i.e., the length between C and C' that $2a$ denotes in Fig. 2(a)). By suitably adjusting this extent, the inverse-square-root stress singularity can be removed. Then, since there are no other singular fields within elasticity satisfying the local boundary conditions (1) or their homogeneous counterparts, the configuration is rendered singularity free. The fact that there are no other singularities follows first from the corresponding eigenvalue equation given in Williams (1952), then from the completeness of the Williams' eigenfunctions for this configuration established in Gregory (1979).

Implicitly this adjustment of contact extent so as to remove the inverse-square-root singularity is what Hertz did (Hertz, 1882). His solution features a contact stress which is nonsingular and, in fact, goes to zero at the edges of the contact region. Stress gradients, on the other hand, are infinite there. To exemplify, for the roller of Fig. 2(a), this Hertzian contact stress is

$$\sigma_c = \frac{4\bar{\sigma}_c}{\pi a}\sqrt{a^2 - x^2}, \tag{3}$$

for $-a \le x \le a$.

The same situation applies for frictionless conforming contact by rigid indentors in general. That is, the extent of the contact region can be adjusted so that only compressive tractions occur within it and there is no interpenetration outside of it. Given compliance with these constraints, stresses are nonsingular. Examples for more extensive conforming contact than that of the roller on the half-space are given in Steuermann (1939) and Persson (1964).

2.2 Conforming Contact with Friction

To obtain a bound on these effects to complement that of frictionless conditions, we can assume that there is no slipping whatsoever while continuing to consider a rigid roller for the time being. The resulting stick conditions within the contact region take the form

$$v = -v_0, \quad u = 0, \quad \text{on} \quad y = 0, \quad x < a. \tag{4}$$

In (4), u is the displacement in the x-direction which is set to zero by virtue of the indented material completely sticking to the rigid indentor. Again the homogeneous counterpart of (4), taken together with the stress-free condition in (1), admits the possibility of stress singularities. From Williams (1952), these are of $\text{ord}(r^{-1/2}\cos(\eta \ln r))$ and $\text{ord}(r^{-1/2}\sin(\eta \ln r))$ as $r \to 0$, where $r = |x - a|$ and $\eta = (1/2\pi)\ln(3 - 4\nu)$, ν being Poisson's ratio. These two singularities occur in combination in *two* distinct local fields which can participate independently of each other (unless $\nu = 1/2$). Thus adjusting the *one* parameter we have available to us, the contact extent, is not sufficient to remove both of them in general. Accordingly, now it can be impossible to find elastic solutions in compliance with (2), and singular stresses can occur. For example, for the rigid roller of Fig. 2(a) but now with stick conditions as in (4), the contact stress becomes

$$\sigma_c = \frac{4\bar{\sigma}_c}{\pi a}\left[\sqrt{a^2 - x^2}\,\cos\left(\eta \ln\left(\frac{a-x}{a+x}\right)\right) + \frac{2\eta a x}{\sqrt{a^2 - x^2}}\sin\left(\eta \ln\left(\frac{a-x}{a+x}\right)\right)\right], \tag{5}$$

for $-a < x < a$.[2] The contact shear is similarly singular. Hence under these conditions, conforming contact does have a stress singularity.

To alleviate the singular response of direct conforming contact with no slip, one can allow some lateral displacement. This can be done by applying the load incrementally so that surface material outside the contact region is at least allowed to move laterally prior to coming into contact. Mossakovskii (1954) describes the implementation of such a physically more realistic approach. Results are nonsingular and comply with the constraints of (2). Indeed, for the contact stress, σ_c is as in (5) but with $\eta = 0$, so that the Hertzian contact stress of (3) is recovered. However, in the limit as the edge of the contact region is approached from within, the ratio of the shear contact stress divided by the normal approaches infinity. This implies an infinite coefficient of friction is needed if no slip is to occur once contact is made. This in turn suggests that we entertain the possibility of slip in the outer portions of the contact region itself.

For such slip under a rigid indentor up to the contact limit at C in Fig. 2(a), the boundary conditions under Amonton's law take the form

$$v = -v_0, \quad \tau_{xy} = \mu\sigma_y, \quad \text{on} \quad y = 0, \quad x < a. \tag{6}$$

In (6), μ is the coefficient of friction. The condition in (6) with the first of (1) prescribe local boundary conditions for a *slip-to-free* transition: when taken abutting the displacement requirements in (4) if $\tau_{xy} < \mu\sigma_y$, they prescribe local boundary conditions for a *slip-to-stick* transition. For both transition configurations it is possible to show only a single singularity exists (the analysis is similar to that in Williams, 1952, and relies on completeness implied in Gregory, 1979). Accordingly, by appropriately adjusting the positions of these two transitions, both singularities can be removed. To capture the physics better, the loading needs to continue to be applied

[2] The derivation of (5) is straightforward using complex potential methods as in Gladwell (1980), Ch. 4.

incrementally (or effectively so via similarity arguments). Such an analysis may be found in Spence (1975) and produces singularity-free stresses.

In closing this section, we consider deformation of the indentor, previously taken as rigid. Results remain essentially the same. For conforming contact without friction, or with friction but allowing for slip, physically reasonable inequalities can be complied with by adjusting boundary region extents and configurations thereby rendered free of singularities. Dundurs and Comninou (1979) furnishes asymptotic arguments that obeying such inequality constraints removes singular behavinr, whilst there are a number of examples showing that one can actually adjust extents to do this (see, e.g., Johnson, 1985).

In sum, therefnre, when sufficient degrees of freedom are available to enable compliance with the pertinent inequalities, stress singularities can be removed from conforming contact problems. The resulting nonsingular stress distributions have been found to be generally supported by experiments (see Johnson, 1985, Ch. 4). Consequently, in these circumstances the stress analyst should make every effort to comply with the inequality conditions. Furthermore, these are the circumstances that apply in dovetail attachments. The key, then, to gauging that one has in fact complied with contact inequalities in numerical solutions is *spatial convergence* (i.e., convergence with grid refinement).

3. FINITE ELEMENT ANALYSIS

3.1 Problem Description

We exploit the symmetry of the configuration to consider only half of the attachment. We denote the two reginns within this half by $\Re_b$ and $\Re_d$ for the blade and disk, respectively (Fig. 1(a)). We take the boundary of $\Re_b$, $\partial_b\Re$, to be comprised of the points $P_1'-P_3'$ and C, C', and the boundary of $\Re_d$, $\partial_d\Re$, to be comprised of the points P_1-P_4 and C, C' (Fig. 1(a)). We use local coordinates (s, n) with origin O_s in the contact region to state the key contact conditions and to present results. For this system, s is the arc length along the surface of the disk starting from a point just outside of the contact region at maximum load and has a corresponding unit vector $\mathbf{e}_s$, while n is the distance locally perpendicular to s and has a unit vector $\mathbf{e}_n$ (Fig. 1(b)). With these geometric preliminaries in place, we can formulate the problem as follows.

In general, we seek the plane strain stresses, $\sigma_s, \sigma_n, \tau_{sn}$, and their associated displacements u_s, u_n, throughout $\Re_b$ and $\Re_d$ satisfying: the stress equations of equilibrium including the body force field produced by the centripetal acceleration of the components; the stress-displacement relations for a homogeneous and isotropic, linear elastic solid in a state of plane strain; the symmetry conditions nn the centerline P_3-P_2' prohibiting transverse displacement and setting the shear stress to zero there; the periodic conditions on the line P_1-P_2 which also prohibit transverse displacement and set shear to zero; an applied radial displacement and zero shear stress on the line P_2-P_3 reflecting the expansion of the disk due to rotation; the applied stress conditions on the end of the blade between points $P_1'-P_2'$ which apply a tension σ_0 in the absence of shear, where σ_0 represents the pull of the unmodelled section of the blade due to its rotation; the stress-free conditions on $\partial_b\Re$ between the points P_1' and C' and between C and P_3'; the stress-free conditions on $\partial_d\Re$ between the points P_1 and C' and between C and P_4; the *contact conditions* on $C-C'$ matching normal and shear contact stresses on the blade and the disk, σ_n^b and σ_n^d as well as τ_{ns}^b and τ_{ns}^d, matching normal displacements, u_n^b and u_n^d, and applying Amonton's law,

$$\sigma_n^b=\sigma_n^d=\sigma_C,\quad \tau_{ns}^b=\tau_{ns}^d=\tau_C,$$

$$u_n^b=u_n^d, \tag{7}$$

$$u_s^b=u_s^d \quad \text{if} \quad \tau_C<\mu\sigma_C,\quad \tau_C=\mu\sigma_C \quad \text{otherwise;}$$

and finally the *contact constraints* requiring that the contact stress be nowhere tensile and prohibiting interpenetration

$$\sigma_C\le 0 \quad \text{for} \quad s_C<s<s_C+2a,$$

$$u_n^b<u_n^d+\frac{(s-s_C)^2}{2R} \quad \text{for} \quad s<s_C, \tag{8}$$

$$u_n^b<u_n^d+\frac{(s-s_C-2a)^2}{2R} \quad \text{for} \quad s>s_C+2a,$$

where s_c is the s coordinate of C (Fig. 1(b)). In particular, we seek the peak stresses occurring at the edge of contact.

Actual input values for the foregoing problem are as follows. The maximum applied stress σ_0 is about 1/6 GPa. The angular velocity is approximately 900 rad/sec at maximum load. This increases the effective applied stress by about ten percent. It is this increased applied stress, $\sigma_0' = 1.1\,\sigma_0$, that is used to normalize stress results subsequently. Material constants used are for density, Young's modulus and Poisson's ratio. Both the disk and the blade are made of a titanium alloy so that these material constants are taken accordingly (see, e.g., Gere and Timoshenko, 1991, App. H). To provide bounds on the effects of friction we take $\mu = 0$ and $\mu = 0.4$, the latter being suggested in Hamdy and Waterhouse (1981) as a likely upper bound for dovetail attachments made of titanium alloys.

3.2 Global FEA

To police (8), we use the point-to-surface contact elements of ANSYS (1995), CONTAC 48. Following ANSYS (1995) recommendations for the analysis of contact problems, these are used in conjunction with ANSYS four-node quadrilateral elements, PLANE 42.

There are some input parameters required to run CONTAC 48 elements. Here we take these to be:

$$h/100 \le \text{TOLN} \le h/50,$$
$$\text{KN} = E, \quad \text{KT} = E/100, \tag{9}$$

where E is the Young's modulus of the titanium alloy and h continues as the mesh size in the contact region. The parameters in (9) let the iterative scheme for the contact elements converge fairly quickly, thereby policing the contact inequalities (8). Typically results are reasonable (free of interpenetration, one-element stress spikes, segments wherein the contact shear is zero when it should not be, etc.). On the few occasions in which the iterative scheme did not converge to sensible results, decreasing TOLN and increasing KN and KT all by a factor of ten completely removed any such problems, albeit at the expense of longer run times. For the number of load substeps required, we take 10, 20 and 40 to check for any sensitivity. We find no differences between results for 20 and 40 for a number of analyses and so take 20 throughout the remainder of the analysis.

To address the issue of *spatial convergence*, we begin with a series of three global grids: a coarse grid (C), a medium (M), and a fine (F). Each of these grids has a boundary layer in the contact region in which we have a uniform mesh (see, e.g., Fig. 3(a), (b)). We take the depth of this boundary layer to be one-fourth of the radius of curvature, this value being found to be adequate in numerical experiments on Hertz-like contact problems. Within this boundary layer, grid refinement is systematic with element edge lengths being successively halved to produce refined grids. Outside of the boundary layer, we approximately systematically refine our grids. We do this by specifying refined element edge lengths at a few locations in the far field and then use the AMESH command of ANSYS (1995) to automatically mesh the rest of the region.

For these first three grids, the actual mesh sizes in the contact region together with the numbers of spatial and contact elements are given in the upper half of Table 1. The mesh size for the coarse grid is as small as any we could discern in the literature reporting FEA of dovetail attachments cited earlier. For the medium and fine grids it is reduced by factors of two and four. Element numbers increase consequently, though not as systematically because of the use of the AMESH automatic mesh generator away from the contact region, and because of some economies made in the use of contact elements in going from the medium to the fine grid.

For this fairly systematically refined sequence of three grids, we take as our criterion for any peak contact stress component σ_{max} to be *converging* that

$$\left|\sigma^{C}_{max} - \sigma^{M}_{max}\right| > \left|\sigma^{M}_{max} - \sigma^{F}_{max}\right|, \tag{10}$$

where the superscripts distinguish grids used. Some justification for convergence checks of this genre is given in Sinclair (1998a).

If (10) is not satisfied, we can proceed with a yet further refined grid to see if we can obtain converging stresses. Specifics of such a superfine grid (S) are also included in Table 1. Again h is halved. Then (10) can be checked for the upgraded set of grids, M, F, and S. This is not an attractive option, however, in terms of computational effort. While the coarse grid runs in under half an hour and even the fine grid runs in about eight hours, the superfine typically takes over forty.[3] Instead, therefore, we turn to submodeling when (10) is not satisfied on our initial three-grid sequence.

Table 1: Summary of Finite Element Grids

Grid	Mesh size in contact region, h/R	No. of spatial elements	No. of contact elements
Coarse global (C)	0.156	915	2,048
Medium global (M)	0.078	2,604	8,462
Fine global (F)	0.039	8,314	t1,711
Superfine global (S)	0.020	22,812	40,667
Coarse submodel (CS)	0.020	768	3,181
Medium submodel (MS)	0.010	3,072	12,697
Fine submodel (FS)	0.005	12,288	50,368

3.3 Submodel FEA

We view global results in deciding where peak contact stresses occur and pick a submodel region which includes these stresses. This results in the shaded submodel region shown in Fig. 3(b). Within this region, grids are uniformly meshed (Fig. 3(c)), and consequently can be fully systematically refined. The first submodel grid (CS) has elements sized the same as for the superfine global grid in this region. Successively halving element sides then produces a medium submodel grid (MS) and a fine (FS). Other specifics of the three-grid sequence for the submodel region are given in the lower half of Table 1.

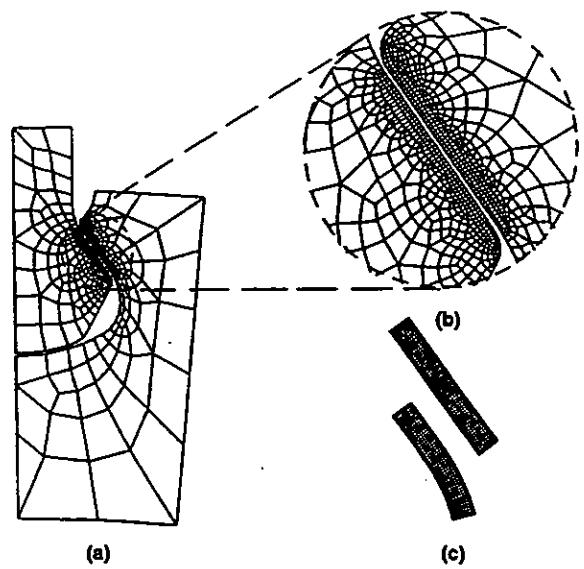

Fig. 3: Finite element grids:
(a) coarse global grid, (b) close-up of coarse global grid with submodel region shown shaded, (c) coarse submodel grid

[3] Run times are for an HP 780 workstation with 720 MB of RAM.

Computational savings with the submodeling are significant. Run times for the coarse submodel grid are two orders of magnitude less than for the superfine global grid, even though they share a common mesh size in the contact region. Run times for the fine submodel grid are somewhat shorter than those for the fine global grid, and consequently quite manageable. This is in marked contrast to the run times to be expected with a global grid of the same resolution in the contact reginn.

In running submodel grids, some of the boundary conditions applied must use values drawn from the global analysis. To ensure that the submodel analysis actually is converging to the correct response for the original global problem, any errors in such boundary conditions must effectively be zero. The steps taken to realize this goal in the submodeling procedure used here are described in Cormier et al. (1999). In brief they are as follows.

First, *displacements* are chosen as the quantities to be taken from global grids for use in boundary conditions for submodel grids. This is because they converge more rapidly than stresses. For four-node quadrilateral elements, Strang and Fix (1973) has

$$e_u = O(h^2), \quad e_\sigma = O(h), \quad \text{as } h \to 0, \tag{11}$$

where e_u, e_σ are the errors in displacements, stresses, respectively.

Second, *nodal* values of displacements are taken from global grids. This is because experience with FEA on test problems demonstrates that typically these displacements are more accurately determined than displacements between nodes (see, e.g., Cormier et al., 1999).

Third, a *cubic spline* is fitted through nodal displacements from global grids to furnish the intervening displacement values needed to run submodel grids. This is because cubic splines are once continuously differentiable throughout their lengths in common with the elastic displacement fields they are trying to replicate.[4]

Fourth, the so-fitted displacements are submitted to a three-grid check analogous to (10). This is to see if these displacement boundary conditions are *converging*.

Fifth and last, a single submodel grid is run with displacement boundary conditions from two successive global grids and peak stresses compared to see that effectively there are no differences between the two evaluations. This is to see if these displacement boundary conditions have *converged*. We provide the results of such a check next in Section 4, after we examine the spatial convergence issue.

[4]This is in contrast to the practice in some standard FEA codes. They use element interpolants which are not, in general, continuously differentiable at nodes. Such discontinuities can be shown to lead to spurious logarithmic stress singularities on submodel boundaries (Sinclair, 1998b).

4. VERIFICATION OF FEA

4.1 Spatial Convergence Checks

Here we examine the convergence of the contact stress σ_c, the contact shear τ_c, and the hoop stress σ_h. We do this initially with a series of plots of stress distributions at maximum load (Figs. 4, 5). In these plots, stresses are normalized by σ'_0, the total applied stress, while arc length s is normalized by s', the distance between O_S and O'_S in Fig. 1(b). This distance slightly exceeds $2a$, the length of the attachment flats and initial contact region. This is so that, when s/s' ranges from 0 to 1, it encompasses the entire coatact region, even with the expanded contact present at maximum load. In addition, we tabulate peak stress values for various grids at maximum load (Table 2).

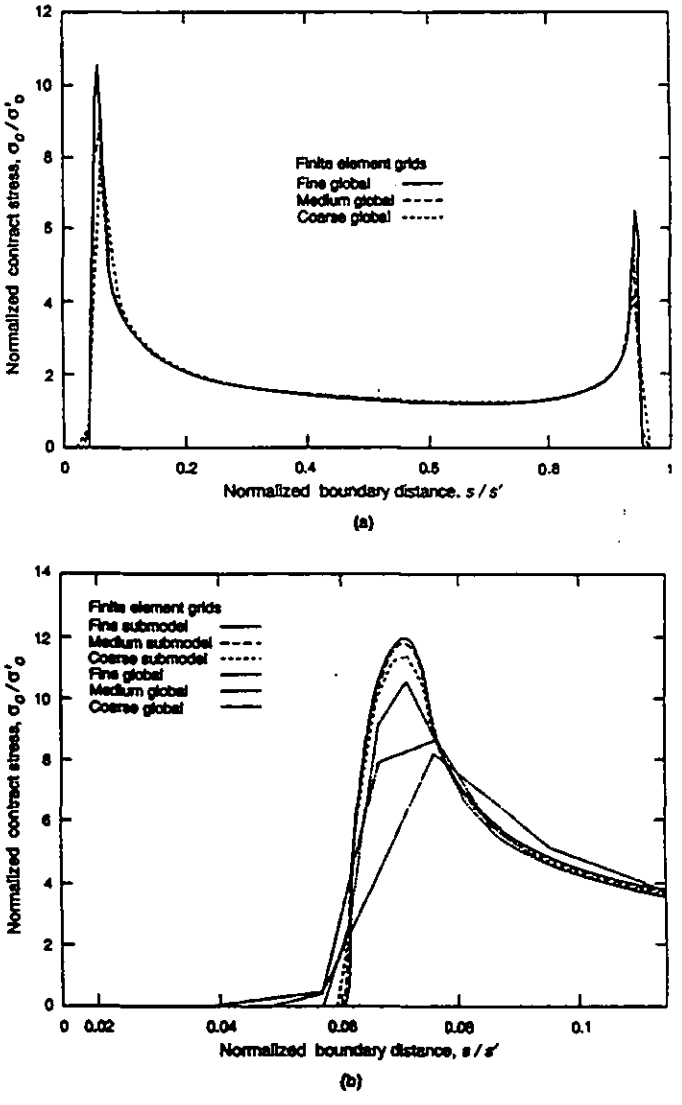

Fig. 4: Convergence of contact stress ($\mu = 0$):
(a) global distributions (from global grids),
(b) local distributions (including submodel results)

The highest magnitudes of σ_C at maximum load occur under frictionless conditions. We view their convergence in Fig. 4. In Fig. 4(a), global grid results are presented. These are converging in the interior of the contact region, results from different grids being indistinguishable there. They are not converging, though, near the edges of contact. This is more clearly shown in Fig. 4(b) which shows peak σ_C for the three global grids. It shows peak σ_C for the three submodel grids as well. These last are converging. This can be confirmed by substituting results from the first column of stresses in Table 2 into checks like (10). Similar results apply for σ_C when there is friction (see the third column of stress results in Table 2).

Table 2: Normalized Peak Stresses at the Edge of Contact

Grid	Stresses without friction		Stresses with friction ($\mu = 0.4$)		
	σ_c/σ'_0	σ_h/σ'_0	σ_c/σ'_0	τ_c/σ'_0	σ_h/σ'_0
C	8.26	-5.24	5.22	2.00	3.41
M	8.63	-7.12	5.93	2.26	4.10
F	10.6	-8.93	7.66	2.93	4.88
CS	11.4	-10.4	8.52	3.26	6.05
MS	11.8	-11.0	8.85	3.41	7.13
FS	12.0	-11.4	9.0	3.48	7.95

Similar results also apply for τ_C. That is, contact shears converge on global grids in the interior of the contact region, but not at the edges of contact. Here submodel results are needed to achieve convergence. This is illustrated in Fig. 5(a) and confirmed by the fourth column of stress results in Table 2.

Without friction, σ_h values are actually converging on the global grid sequence, albeit slowly (see second column of stress results in Table 2). With friction, though, convergence of σ_h is more difficult to achieve. In fact, σ_h for the grid sequence M, F, CS does not satisfy its version of (10) (see Fig. 5(b) and the last column of Table 2). However, σ_h on the grid sequence F, CS, MS is converging, as it is on the sequence CS, MS, FS. Hence, provided submodel results are used, *all* peak stresses at the edge of contact are *spatially converging*.

To begin to assess the level of accuracy peak stresses have converged to, we adopt the error estimate e calculated by

$$e = \left|\sigma_{max}^{MS} - \sigma_{max}^{FS}\right| / \left|\sigma_{max}^{FS}\right|, \qquad (12)$$

and expressed as a percentage. In (12), σ_{max} continues as the peak value of any one of the stresses σ_C, τ_C, σ_h, and the superscript identifies the grid used to compute it.

Given stresses converging linearly with h as in (11), e of (12) is the appropriate error estimate. Here, however, stresses do not uniformly comply with (11). This is because, in addition to resolving the stress gradients present, the FEA is attempting to resolve the extent of the contact region. The latter activity can result in somewhat erratic convergence. The situation is akin to finding a root of an equation with a bisection algorithm: while this algorithm must ultimately converge if the root is not repeated, successive estimates of the root themselves do not have to move monotonically closer to the true answer.

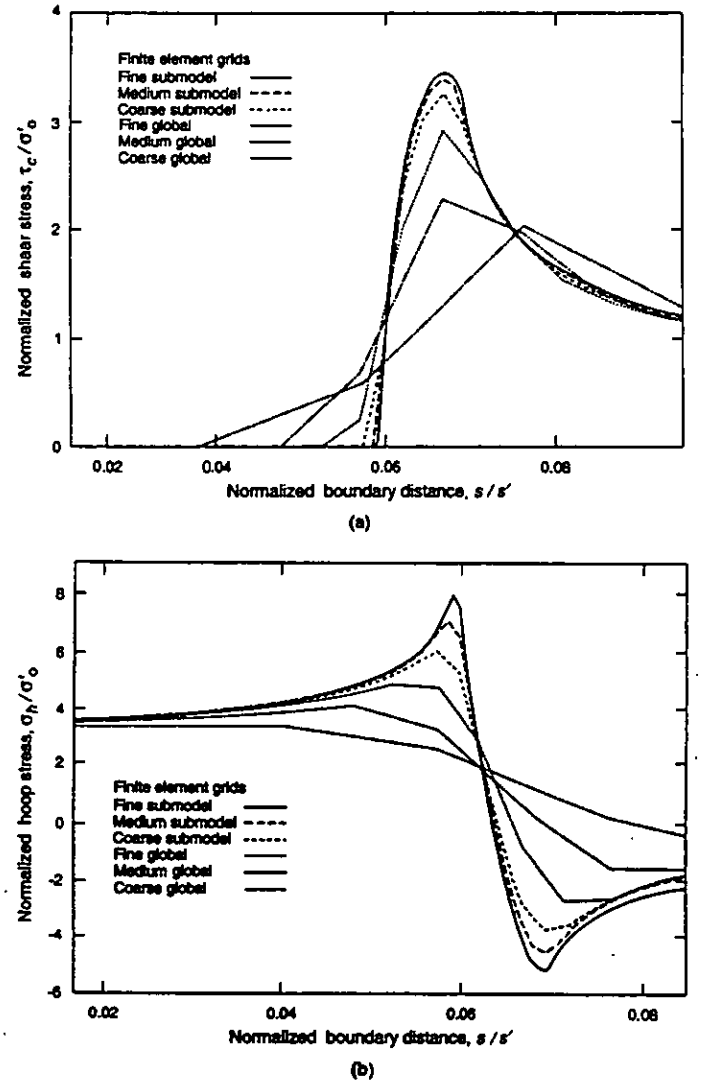

Fig. 5: Convergence of other stress components ($\mu = 0$): (a) local shear stresses, (b) local hoop stresses

Typically convergence difficulties associated with determining the extent of contact diminish with increasing grid refinement. This is illustrated on the s/s' axes in Figs. 4(b), 5(b). It is also reflected in the stresses in Table 2. Eventual compliance with (11) implies differences between CS and MS stresses are twice those between MS and FS stresses. For the most part in Table 2, this halving of differences holds at least approximately.

The stress that deviates the most from ultimately complying with (11) is σ_h when $\mu = 0.4$. This is because there is an abrupt change in the slope of the hoop stress at the edge of contact in the presence of friction (see Poritsky, 1950). Consequently the FEA has the further

task of positioning this sharp peak in σ_h (see Fig. 5(b)). This positioning slows convergence and compliance with (11). However, in lieu of anything obviously superior, we continue to use e of (12) for our error estimate.

Applying (12) to Table 2 results in the following error estimates: for σ_c and $\mu = 0$ or 0.4, $e = 1.7(\%)$; for τ_c, $e = 2.0(\%)$; for σ_h ($\mu = 0$), $e = 3.5(\%)$; and for σ_h ($\mu = 0.4$), $e = 10(\%)$. Hence for the most part, *spatial convergence* to good levels of accuracy is realized (< 5%). To improve the one instance of merely satisfactory convergence (10%), a further submodel within our subregion is needed. We do not undertake this in the present study. Cormier et al. (1999) describes how to effect such successive submodeling, and demonstrates on a test problem the sort of improved accuracy that can be so realized.

4.2 Other Checks

Here we summarize checks on submodel boundary conditions, compliance with Amonton's law, and convergence with unloading.

For the *check on submodel boundary conditions*, the medium submodel grid is used to calculate peak contact stresses when displacements are taken from the medium, fine and superfine global grids. To keep computation down, this is only done for the frictionless case. Results for peak σ_c/σ'_0 with these respective grids furnishing boundary conditions are: 12.5, 11.8, 11.5. Here differences between successive σ_c/σ'_0 are approximately halving, so that it is reasonable to take the difference between the first two as a measure of the error in results reported here from this source. This yields an estimate of 5.9 percent, higher than what one would want for a good level of accuracy. However, this error is associated with an overestimate of σ_c/σ'_0, whereas the earlier error estimate e is associated with an underestimate. Consequently the two cancel to a degree and give an overall error estimate within the five percent limit for a good level of accuracy. The same sort of cancellation occurs for the hoop stress under frictionless conditions and is expected to occur for results when friction is present, thereby effectively leaving accuracy levels unimpaired by errors in submodel boundary conditions.

To *check on Amonton's law*, we first observe that a flag in the ANSYS code indicates that all nodes in the contact region should be slipping during loading up. Therefore the contact conditions (8) have $\tau_c = \mu\sigma_c$ throughout contact. To see if this is so, Fig. 6 plots τ_c and $\mu\sigma_c$. For most of the global distributions, the two are indistinguishable (Fig. 6(a)). At the edge of contact, there are some differences (Fig. 6(b)). For the peak values, τ_c is 3.3 percent low (Table 2). This underestimate of τ_c may well be offset in large part by an overestimate resulting from submodel boundary conditions, so that it seems likely that the error remains fairly close to the corresponding e of Section 4.1 (2.0%), and that overall accuracy levels for τ_c are still good.

For *checks on unloading*, we consider two loading histories. The first completely unloads the attachment under frictionless conditions. Theoretically, response at any load level under these conditions should be independent of whether one is loading up or down. The FEA results for all grids agree with this prediction to within 0.5 percent. The second loading history cycles the loading down then back up after reaching maximum load. Friction is present for these load cycles. For a fixed unload increment, a steady-state response can be expected to be realized under these circumstances. The FEA results stabilized after two cycles to three significant figures.

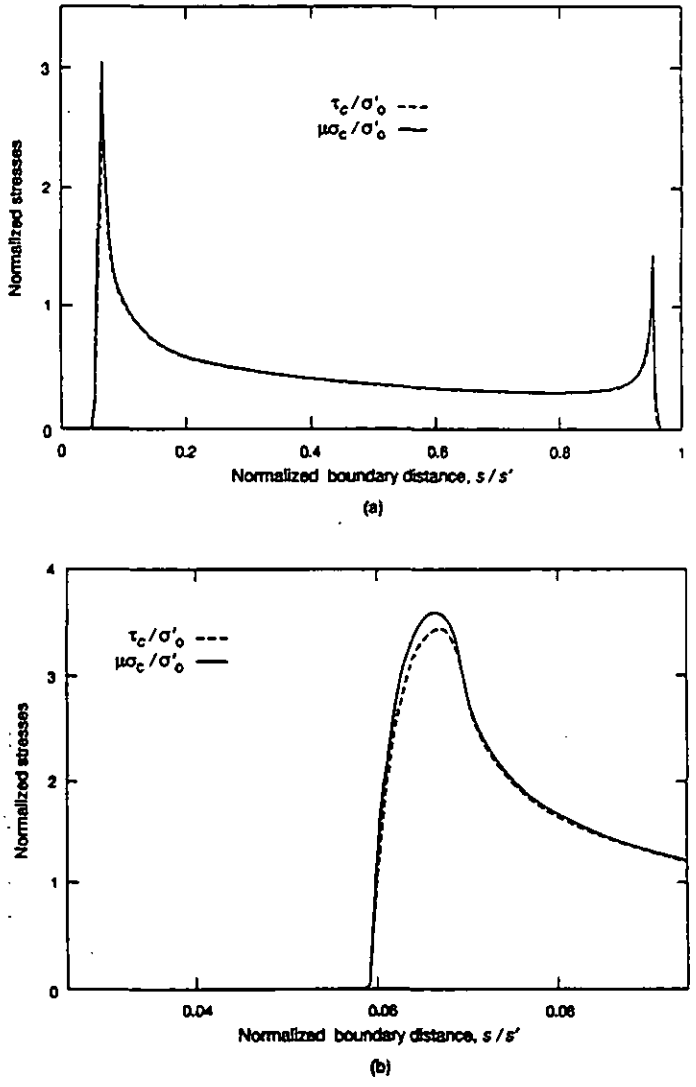

Fig. 6: Comparison of shear stress with limiting value (t_c cf. $\mu\sigma_c$, $\mu = 0.4$):
(a) global comparison (from fine global grid),
(b) local comparison (from fine submodel grid)

In sum, therefore, the finite element analysis described here is in good agreement with all additional checks.

5. CONCLUDING REMARKS

The conforming contact occurring in dovetail attachments does *not* lead to *singular* stresses. This is so with or without friction effects

being present. That stresses are finite can be shown via asymptotic analysis (Section 2). It follows that finite element analysis of dovetail attachments should produce converging stresses. In fact, converging stresses can be realized if *contact elements police* the required *contact constraints*. The point-to-surface contact elements used here (CONTAC 48 of ANSYS, 1995) are quite capable of the requisite policing. This is demonstrated in this study with and without friction (Table 2).

Although the contact stresses in dovetail attachments are finite, they are large near the edges of contact and do possess *high stress gradients* there. Furthermore, it is necessary to *position* the *edges of contact* themselves with some precision if contact constraints are to be satisfied. Consequently if one is to accurately capture stresses near the edges of contact in dovetail attachments with finite elements, one can expect to need a *highly refined mesh* in this vicinity ($h \sim R/100$). The submodeling procedure described here (Section 3.3) appears ultimately to provide a mesh of sufficient resolution, and to do so in return for moderate computational effort. To achieve good levels of accuracy for peak stresses near the edges of contact, the mesh sizes required are considerably smaller than those in cited earlier analyses.

Two final observations are in order. First we observe that the somewhat erratic convergence which can occur initially in conforming contact problems can mislead a stress analyst into thinking stresses have converged when they have not. To see this, suppose one adopted a two-grid convergence check and viewed a change of five percent as acceptable. Then from the first two global grids used to analyze the dovetail here, one would conclude that the peak normalized contact stress is 8.63 under frictionless conditions (Table 2). In fact this estimate is low by about forty percent of its value. While the three-grid check used in this paper does not guarantee that one could nnt make such a nonconservative estimate, it does prevent it happening here and can be expected to make it less likely for other conforming contact configurations.

Second we observe that it should not be thought that the smoothing of stress gradients which accompanies plastic flow obviates the stress analyst from accurately resolving elastic stress fields if accurate elasto-plastic stresses are sought. Basically this is because elastic response physically precedes and triggers elasto-plastic. To explain further, using the fine submodel grid, local first yielding for the dovetail without friction is predicted to occur when loads attain 58 percent of the maximum value used here (based on a Tresca yield criterion). Using just the coarse global grid, this event is not predicted to occur until loads reach 84 percent of their maximum value. Clearly a significant erroneous delay results from using a finite element mesh of insufficient refinement.

ACKNOWLEDGMENTS

We are pleased to acknowledge the benefit of technical discussions with engineers at General Electric Incorporated. We are also grateful for the financial support of this work by General Electric Aircraft Engines.

REFERENCES

ANSYS personnel, 1995, *ANSYS User's Manual*, Revision 5.2, Vol. I, ANSYS Incorporated, Canonsburg, Pennsylvania.

Boddington, P.H.B., Chen, K., and Ruiz, C., 1985, "The Numerical Analysis of Dovetail Joints," *Computers and Structures*, Vol. 20, pp. 731-735.

Cormier, N.G., Smallwood, B.S., Sinclair, G.B., and Meda, G., 1999, "Aggressive Submodelling of Stress Concentrations," *International Journal for Numerical Methods in Engineering*, to appear (advance copies are available from the third author).

Dundurs, J., and Comninou, M., 1979, "Some Consequences of the Inequality Conditions in Contact and Crack Problems," *Journal of Elasticity*, Vol. 9, pp. 71-82.

Gere, J.M., and Timoshenko, S.P., 1991, *Mechanics of Materials*, 3rd SI ed., Chapman & Hall, London.

Gladwell, G.M.L., 1980, *Contact Problems in the Classical Theory of Elasticity*, Sijthoff and Noordhoff International Publishers, Alphen aan den Rijn, The Netherlands.

Gregory, R.D., 1979, "Green's Functions, Bi-Linear Forms, and Completeness of the Eigenfunctions for the Elastostatic Strip and Wedge," *Journal of Elasticity*, Vol. 9, pp. 283-309.

Hamdy, M.M., and Waterhouse, R.B., 1981, "The Fretting Wear of Ti-6A1-4V and Aged Inconel 718 at Elevated Temperatures," *Wear*, Vol. 71, pp. 237-248.

Hertz, H., 1882, "On the Contact of Elastic Solids," *Journal für die reine und angewante Mathematik*, Vol. 92, pp. 156-171 (in German: for an account in English, see Johnson, 1985, Ch. 4).

Johnson, K.L., 1985, *Contact Mechanics*, Cambridge University Press, Cambridge, U.K.

Kalker, J.J., 1977, "A Survey of the Mechanics of Contact Between Solid Bodies," *Zeitschrift für angewandte Mathematik und Mechanik*, Vol. 57, pp. T3-T17.

Kenny, B., Patterson, E.A., Said, M., and Aradhya, K.S.S., 1991, "Contact Stress Distributions in a Turbine Disk Dovetail Type Joint – a Comparison of Photoelastic and Finite Element Results," *Strain*, Vol. 27, pp. 21-24.

Meda, G., and Sinclair, G.B., 1996, "A Survey of Some Recent Papers in Contact Mechanics," Report SM 96-7, Dept. of Mechanical Engineering, Carnegie Mellon University, Pittsburgh, Pennsylvania.

Meguid, S.A., Refaat, M.H., and Papanikos, P., 1966, "Theoretical and Experimental Studies of Structural Integrity of Dovetail Joints in Aeroengine Discs," *Journal of Materials Processing Technology*, Vol. 56, pp. 668-677.

Mossakovskii, V.I., 1954, "The Fnndamental Mixed Problem of the Theory of Elasticity for a Half-Space with a Circular Line Separating the Boundary Conditions," *Prikladnaia Matematika i Mekhanika*, Vol. 18, pp. 187-196 (in Russian).

Papanikos, P., and Meguid, S.A., 1994, "Theoretical and Experimental Studies of Fretting-Initiated Fatigue Failure of Aeroengine Compressor Discs," *Fatigue and Fracture of Engineering Materials and Structures*, Vol. 17, pp. 539-550.

Papanikos, P., Meguid, S.A., and Stjepanovic, Z., 1998, "Three-Dimensional Nonlinear Finite Element Analysis of Dovetail Joints in Aeroengine Discs," *Finite Elements in Analysis and Design*, Vol. 29, pp. 173-186.

Persson, A., 1964, "On the Stress Distribution of Cylindrical Elastic Bodies in Contact," Doctoral Dissertation, Chalmers University of Technology, Göteborg, Sweden.

Poritsky, H., 1950, "Stresses and Deflections of Cylindrical Bodies in Contact," ASME JOURNAL OF APPLIED MECHANICS, Vol. 17, pp. 191-196.

Sadowsky, M.A., 1928, "Two-Dimensional Problems of Elasticity Theory," *Zeitschrift für angewandte Mathematik und Mechanik*, Vol. 8, pp. 107-121 (in German).

Sinclair, G.B., 1998a, "FEA of Singular Elasticity Problems," *Proceedings of the Eighth International ANSYS Conference*, Pittsburgh, Pennsylvania, Vol. 1, pp. 225-236.

Sinclair, G.B., 1998b, "On the Logarithmic Stress Singularities Induced by the Use of Displacement Interpolants as Boundary Conditions in Submodelling," Report SM 98-5, Dept. of Mechanical Engineering, Carnegie Mellon University, Pittsburgh, Pennsylvania.

Spence, D.A., 1975, "The Hertz Contact Problem with Finite Friction," *Journal of Elasticity*, Vol. 5, pp. 297-319.

Steuermann, E., 1939, "To Hertz's Theory of Local Deformations in Compressed Elastic Bodies," *Comptes Rendus (Doklady) de l'Académie des Sciences de l'URSS*, Vol. 25, pp. 359-361.

Strang, G., and Fix, G.J., 1973, *An Analysis of the Finite Element Method*, Prentice-Hall, Inc., Englewood Cliffs, New Jersey.

Williams, M.L., 1952, "Stress Singularities Resulting from Various Boundary Conditions in Angular Corners of Plates in Extension," ASME JOURNAL OF APPLIED MECHANICS, Vol 19, pp. 526-528.